J Nanopart Res (2013) 15:1632
DOI 10.1007/s11051-013-1632-3

RESEARCH PAPER

Controlled synthesis of VO_2(R), VO_2(B), and V_2O_3 vanadium-oxide nanowires

Jhih-Syuan Ke · Sheng-Feng Weng · Ming-Cheng Wu · Chi-Shen Lee

Received: 21 March 2012 / Accepted: 2 April 2013 / Published online: 13 June 2013

Abstract Vanadium-oxide nanowires (NWs) V_2O_5, VO_2(R), VO_2(B), and V_2O_3 are deposited on a substrate to study their field-emission properties. V_2O_5 NWs are prepared by thermal evaporation via vapor transport of a vanadium-oxide complex under mild conditions. Films of VO_2 and V_2O_3 wires are subsequently prepared by reducing V_2O_5 one-dimensional nanocrystals at 450 °C with hydrogen gas. The composition of the flowing H_2/Ar mixture and the duration of reduction are utilized to control the formation of VO_2(R) or VO_2(B) NWs. The crystallinity and morphology of products as prepared are characterized using several techniques, including powder X-ray diffraction, a scanning electron microscope, and a transmission electron microscope. The field-emission properties of the vanadium-oxide NWs as prepared exhibit a turn-on field of 4.56–7.65 V/μm and an emission current density up to 3.68–8.36 mA/cm^2. These features indicate that vanadium-oxide NWs have potential FE emitter applications.

Keywords V_2O_5 · VO_2(R) · VO_2(B) · V_2O_3 · Nanowire · Film · Morphology control

Introduction

Metal oxides with a one-dimensional (1D) nanostructure, such as nanobelts, nanorods, nanowires (NWs), and nanotubes, have attracted considerable attention because of their specific physical properties and diverse potential applications in catalytic, photoelectronic, sensor, battery, and thermoelectric devices (Xiong et al. 2008; Jiang et al. 2006, 2011; Li et al. 2006; Wang et al. 2010; Wang and Cao 2007; Li et al. 2010; Ramgir et al. 2010; Fan et al. 2009; Wang 2008; Liu et al. 2008; Wei and Natelson 2011; Zhai et al. 2011). Among these materials, a 1D nanostructure for vanadium oxides with varied oxidation states, including V_2O_5, VO_2, and V_2O_3, shows electronic, thermochromic, magnetic, and optoelectronic properties, which are widely applied in chemical sensors and in electrochromic and thermochromic devices (Zhai et al. 2010; Wang et al. 2008; Liu et al. 2005; Grigorieva et al. 2010; Wee et al. 2010; Yin et al. 2011). In some vanadium-oxide compounds, the unique structural features and structural transformations enable an application of their serving as electrodes in rechargeable lithium batteries (Jiao et al. 2006; Leger et al. 2007).

Vanadium dioxide (VO_2) is a traditional binary compound with several allotropic phases, including

Electronic supplementary material The online version of this article (doi:10.1007/s11051-013-1632-3) contains supplementary material, which is available to authorized users.

J.-S. Ke · S.-F. Weng · M.-C. Wu · C.-S. Lee (✉)
Department of Applied Chemistry, National Chiao Tung University, 1001 University Road, Hsinchu 30010, Taiwan
e-mail: chishen@mail.nctu.edu.tw

VO_2(R), VO_2(B), and VO_2(A). VO_2(R), with a rutile monoclinic structure as the most stable phase, possesses a unique phase transition from semiconductor to metal (SMT) at about 340 K that initiates a phase transition, leading to a transformation of the optical properties, IR penetration, and total reflection (Ji et al. 2010; Guiton et al. 2005). Metastable VO_2(B) exhibits a promising electrochemical performance compared with the well-known binary oxide V_2O_5, which has been increasingly looked at as a candidate for the cathode in lithium-ion batteries (Baudrin et al. 2006). V_2O_3 also undergoes a phase transition from SMT at $\sim$150 K (Morin 1959). After the phase transition, an insulating, antiferromagnetic phase of the monoclinic class converts to a metallic phase with the corundum structure; the electrical resistivity also decreases radically.

Reduced vanadium-oxide NWs are synthesized using several methods. A common preparation of vanadium-oxide NWs involves a hydrothermal treatment of the vanadium precursor with a reducing agent. For example, Sediri et al. (2006) reported the use of aniline as both the reducing agent and the structural templating agent to prepare VO_2(B) nanoneedles from bulk V_2O_5 powder. Yin et al. (2011) reported a hydrothermal method to synthesize bundle-like VO_2(B) NWs, followed by heat-treatment process to produce VO_2(M1/R) nanobundles. Ji et al. (2010) fabricated single-crystal VO_2(R) nanorods from the reaction of bulk V_2O_5 powder under hydrothermal treatment in the presence of oxalic acid as the reducing agent and $H_2SO_{4(aq)}$ as the acidifying agent. VO_2(R) with 1D nanostructures was synthesized via PECVD, as reported by Guiton et al. (2005) they deposited VO_2(R) NWs on Si_3N_4 substrates with VO_2(B) powder as a vanadium source under thermal evaporation (900–1,000 °C) with flowing argon as a carrier gas. V_2O_3 1D nanostructures have been synthesized only through reduction from V_2O_5 or VO_2 to V_2O_3. For example, Santulli et al. (2009) prepared VO_2 nanorods with a hydrothermal treatment and reduced it to V_2O_3 in the presence of a reducing gas. Corr et al. (2008) reported a systematic reduction of V_2O_5 nanoscrolls to VO_2(R) and V_2O_3 on adjusting the reduction temperature and reaction period. To our knowledge, there has been no prior study for VO_2(R), VO_2(B), and V_2O_3 NWs deposited on a substrate.

We controlled the growth of nearly aligned MoO_3 and V_2O_5 NWs on various substrates (Wu and Lee 2009a, b), and obtained reduced vanadium-oxide NWs using V_2O_5 NWs, as prepared, on an ITO substrate (Wu and Lee 2009b). In the present study, we performed a systematic investigation of reduction conditions to obtain reduced vanadium oxides as VO_2(R), VO_2(B), and V_2O_3 NWs by adjusting the duration of the reaction or the composition of the reducing gas. Structural information about reduced vanadium-oxide NWs was derived with analytical techniques including scanning electron microscope (SEM), transmission electron microscope (TEM), SAED, X-ray diffraction (XRD), and XPS. We also measured field emission. The results showed small actuation voltages and a large current density for reduced vanadium-oxide NW arrays, properties which would be useful in optoelectronic nanodevices.

Experiments

Synthesis

V_2O_5 NWs were grown on a substrate by means of thermal evaporation (Wu and Lee 2009b). A mixture of V_2O_5 powder (0.1 g, 0.55 mmol) and $NH_2OHH\text{-}Cl_{(aq)}$ (3 M, 2 mL) was placed in a glass vial and stirred at 50 °C. The color of the mixture turned from orange to blue, indicating the reduction of V_2O_5. Thereafter, a glass slide rinsed with ethanol and deionized water covered the top of the glass vial, and this installation was transferred to a programing furnace. The temperature was raised to 400 °C over 1 h; V_2O_5 NWs were grown on the surface of the glass slide. The pure V_2O_5 NW thin film was placed in an alumina crucible in a tube furnace under flowing reducing gas at a flow rate 0.4 standard liter per minute (SLPM). This reduction proceeded at a constant rate of heating, 200 °C/h, and then held at 450 °C. The reaction conditions to obtain pure phases of reduced vanadium oxides are summarized in Table 1.

Characterization

Several analytical techniques were used to confirm the nature of the products as prepared. The crystalline products were subjected to powder XRD (Bruker AXS D8 Advance, Leipzig Germany; operated at 40 kV, 40 mA) with Cu-Kα radiation. The micrographs of a SEM (Hitachi, S-4700I, operated at 15 kV) and a TEM

Table 1 Reduction conditions and refined cell parameters of reduced products as obtained

Product	Conditions of reduction			Refined cell parameters (Å)					
	Composition	T (°C)	Duration (h)	Lattice	Space group	a	b	c	β
VO_2(R)	10 % H_2/90 % Ar	450	12	Monoclinic	$P2_1/c$	5.74 (7)	4.54 (1)	5.35 (8)	122.5 (1)°
VO_2(B)	100 % H_2	450	2	Monoclinic	$C2/m$	12.03 (2)	3.687 (5)	6.4 (1)	106.8 (2)°
V_2O_3	100 % H_2	450	4	Hexagonal	R-3c	4.94 (2)	4.94 (0)	14.019 (7)	–

(JEOL, JEM-3000F, operated at 200 kV) were used to determine the morphology and size of the NWs. The samples for the TEM experiments were prepared as follows. The NWs were separated from glass on ultrasonic dispersion of the thin film in ethanol for 5 min. The dispersion solution was then dropped onto a copper grid (carbon film-coated, 100 mesh), and dried in air leaving the NWs spread on the carbon film. X-ray photoelectron spectra were recorded with a XPS spectrometer (PHI Quantera SXM); the pass energy was 55 eV and the binding energy was calibrated according to the C-1s line at 284.4 eV. The pressure in the chamber was less than 6.7×10^{-7} Pa during the experiment. All spectra were fitted with a XPS peak software package. For measurement of the field emission, the vanadium-oxide thin films were placed in a vacuum chamber near 295 K, and used copper conductive tape to connect the thin film and one of electrode. During the experiment, the pressure of vacuum chamber was kept less than 3×10^{-7} Pa. The distance between the electrode and sample was fixed at 100 μm; a high-voltage source meter (Keithley 2410) was used to measure the current–voltage characteristics. The measurements were performed several times to obtain reproducible results. The measured emission area was 0.785 cm^2, which was adhered to the surface of a copper electrode using silver paint and mounted to a stage with a resistive heater. In the measurement, the turn-on field is determined by extracting the interception of the linear region to the x-axis of a semi-log plot.

Results and discussion

Synthesis and reduction conditions

V_2O_5 NWs thin film were first prepared as a reactive precursor via a route of vapor pyrolysis and deposition on a glass substrate developed previously. The V_2O_5 NWs as prepared were further heated in a tube furnace with H_2/Ar pre-mixed gas as a reducing atmosphere, with controlled composition and flow rate (0.4 SLPM). When we tried to reduce the V_2O_5 thin films with H_2/Ar pre-mixed gas at ambient concentrations, we discovered that VO_2(R) and VO_2(B) appeared only under conditions of H_2 at low and high concentrations. On this basis, we set two reduction conditions to prepare reduced vanadium oxide as a pure phase under mild and rigorous reducing conditions using low and high concentrations of H_2 in Ar pre-mixed flowing gas. Details of the parameters and the results of the reduction conditions are summarized in Table 1 with supporting information (Table S1).

Powder X-ray diffraction

The crystallinity and purity of NWs as prepared were confirmed with powder XRD, as shown in Fig. 1. The XRD profile of the V_2O_5 NW precursor as synthesized was indexed according to an orthorhombic unit cell (JCPDS 41-426, space group: $Pmn2_1$) with refined lattice parameters of $a = 11.45$ (1) Å, $b = 4.430$ (6) Å, and $c = 3.542$ (3) Å. Figure 1b shows the XRD pattern for the product obtained under mild reduction conditions (No. 3), which corresponded to monoclinic rutile VO_2(R) (JCPDS 43-1051). For conditions Nos. 4 and 5, the products were VO_2(B) (Fig. 1c, JCPDS 65-7960) and V_2O_3 (Fig. 1d, JCPDS 84-0312). The refined lattice parameters of all products are summarized in Table 1. The reduction could be regarded as a continuous process and that the vanadium oxide was reduced gradually by hydrogen. The transformation of V^{4+} into V^{3+} occurred immediately after the conversion of V^{5+} to V^{4+}. Vanadium ion V^{4+} was treated as an intermediate during the reduction that could be preserved on limiting the duration of the reaction. Amorphous VO_x was also preserved, and PXRD profiles revealed a small ratio of signal to noise. When the duration of reduction was increased, the

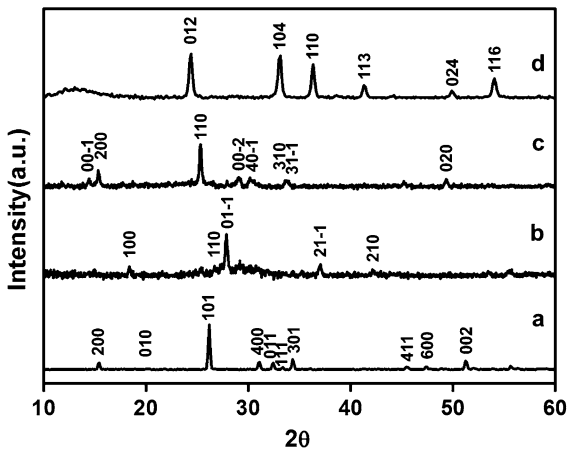

Fig. 1 XRD profiles of (*a*) V_2O_5, (*b*) VO_2(R), (*c*) VO_2(B), and (*d*) V_2O_3

amorphous VO_x species became completely converted to V_2O_3 and crystallized, which resulted in a sharp PXRD pattern.

Morphology and structure

The representative morphology and structure of typical product NWs were investigated with FE SEM and TEM, as shown in Figs. 2 and 3, respectively. Figure 2a shows the SEM image of precursor product V_2O_5 NWs possessed a length up to 30 μm, as calculated from the SEM image. Other SEM images (see Supporting Information, Fig. S1) confirmed the NW structure of V_2O_5 to have a width of 70–150 nm. The side-view image (inset of Fig. 2a) clearly revealed that V_2O_5 NWs were aligned to the surface of the glass. Figure 2b–d shows SEM images of the reduced products; the insets are their corresponding side-view images. The structures of reduced VO_2(R), VO_2(B), and V_2O_3 NWs were essentially similar to that of V_2O_5 NWs as prepared. It was clearly demonstrated that the morphology was not destroyed during the reduction.

Figure 3a shows the TEM image of a single V_2O_5 NW; the insets show its corresponding selected area electron-diffraction (SAED) pattern (top) and high-resolution TEM (HR-TEM) image (bottom). The SAED pattern and HR-TEM image of the single wire were recorded from the [0 1 0] zone axis; the SAED pattern revealed sharp and clean diffraction spots, indicative of a single-crystalline property. The HR-TEM image indicated lattice fringes of spacing 5.72 and 3.39 Å, corresponding respectively to the (2 0 0) and (1 0 −1) crystal planes for orthorhombic V_2O_5. The growth direction was along the *c*-axis, which was deduced from the 90° angle between the *c*- and *a*-axes, consistent with previous study. Figure 3b–d shows

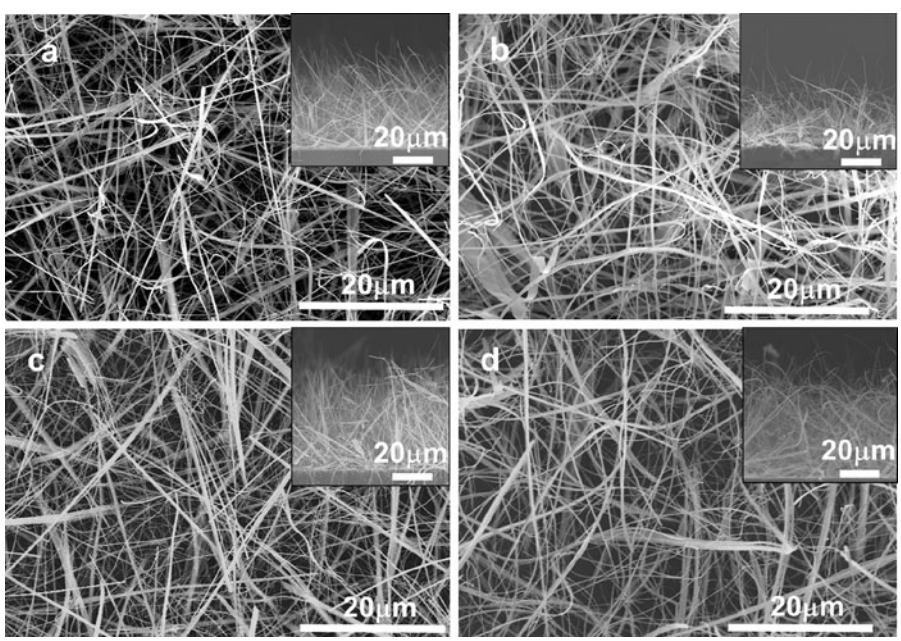

Fig. 2 Top-view SEM images and corresponding side-view images (*inset*) of **a** V_2O_5, **b** VO_2(R), **c** VO_2(B), and **d** V_2O_3 NW thin films

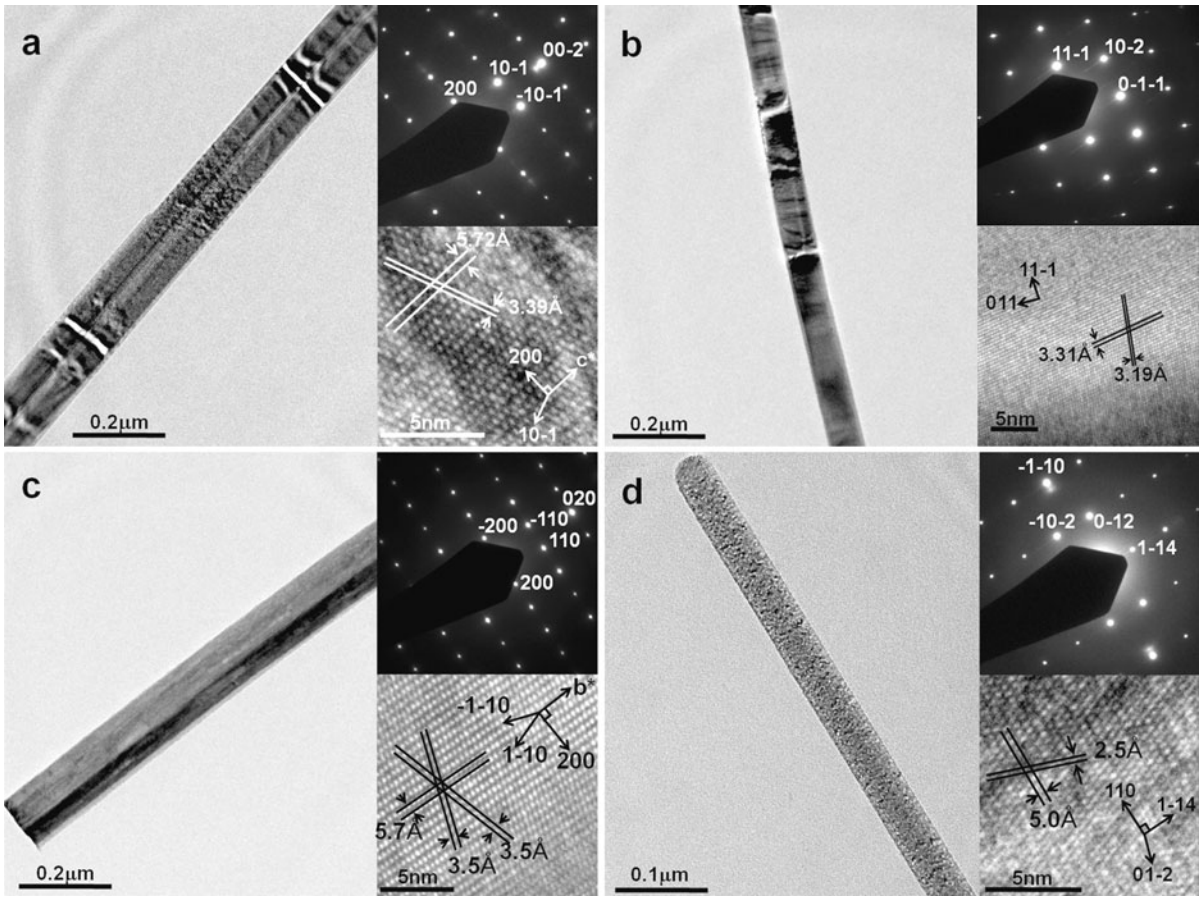

Fig. 3 TEM (*left*), SAED (*right top*), and HR-TEM (*right bottom*) images of **a** V_2O_5, **b** VO_2(R), **c** VO_2(B), and **d** V_2O_3 NWs as obtained, respectively

TEM images of single NWs of reduced products, and the insets show their corresponding SAED patterns (top) and HR-TEM images (bottom). The SAED patterns and HR-TEM images of VO_2(R), VO_2(B), and V_2O_3 single wires were recorded from the zone axes [2 −1 1], [0 0 1], and [2 −2 1], respectively. All SAED patterns of reduced products exhibited sharp and clean diffraction spots owing to the single-crystalline property. The HR-TEM image of a portion of VO_2(R) NW revealed parallel lattice fringes with inter-layer distances of ∼3.31 and 3.19 Å, corresponding to planes (1 1 −1) and (0 1 1). Combined with the TEM image, the growth direction of the VO_2(R) NW was near a vector perpendicular to plane (1 1 −1). The HR-TEM images of VO_2(B) NWs show the *d*-spacings of 3.5 and 5.7 Å, consistent with those of (1 −1 0) and (2 0 0), respectively. The growth direction of VO_2(B) NWs was along the *b*-axis, as deduced from the 90° angle between the *b*- and *a*-axes. As shown in Fig. 3d, the marked interplanar *d*-spacings of 2.5 and 5.0 Å corresponded to the (0 1 −2) and (1 −1 4) lattice planes of hexagonal V_2O_3, respectively. The results of SAED and HR-TEM demonstrated that the V_2O_3 NWs had a single-crystalline structure along a growth direction of the normal vector of plane (1 1 0), deduced using the 90° angle between two normal vectors of planes (1 1 0) and (1 −1 4). The directions of crystal growth of all reduced products were indicated by SAED and HR-TEM analyses, and these were influenced by the conversion of precursor product V_2O_5 NWs.

X-ray photoelectron spectral analysis

XPS analysis was undertaken to investigate the oxidation state of vanadium ions in the products as prepared. As shown in Fig. 4, XPS lines of ∼517 eV ($V2p_{1/2}$) and ∼524 eV ($V2p_{3/2}$), respectively, are assigned to

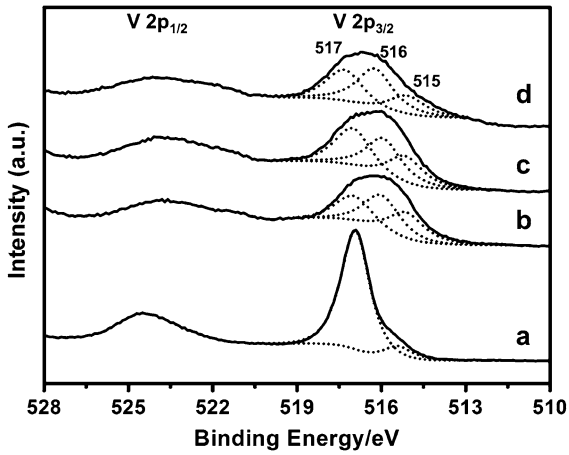

Fig. 4 XPS spectrum in the V-2p region of (*a*) V_2O_5, (*b*) VO_2(R), (*c*) VO_2(B), and (*d*) V_2O_3 NW thin films as prepared, respectively

the BE of V^{n+} in the VO_x NWs. The lines in the $V2p_{3/2}$ spectra of VO_2(R) and VO_2(B) (Fig. 4, lines b and c) were broad, ranging from 514 to 518 eV, indicative of mixed oxidation states of vanadium ions. According to line modeling, the $V2p_{3/2}$ spectrum contained three contributions at 517.02, 515.93, and 515.04 eV, corresponding to V^{5+}, V^{4+}, and V^{3+} ions, indicative of V^{3+} and V^{5+} ions on the surface of VO_2(R) and VO_2(B) NWs. The broad line caused by mixed oxidation states of vanadium ions, V^{5+}, V^{4+}, and V^{3+} ions, was found also in the $V2p_{3/2}$ spectrum of V_2O_3 (see Fig. 4, line d). The appearance of V^{5+} and V^{4+} ions might have been due to the oxidation of

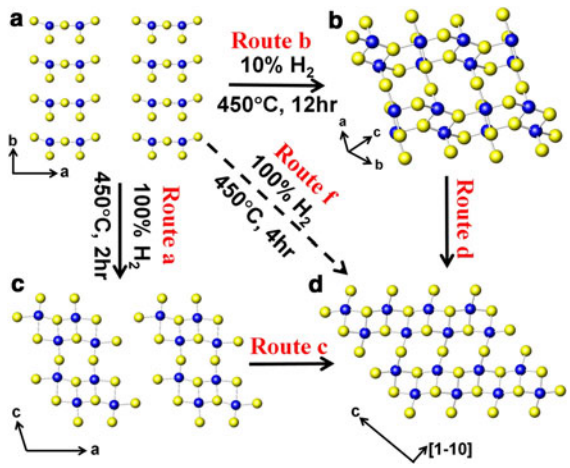

Fig. 5 Schematic illustration of transformative evolution, showing single atomic layers of (*a*) V_2O_5, (*b*) VO_2(R), (*c*) VO_2(B), and (*d*) V_2O_3 along their corresponding growth planes

vanadium ions at the surface of the NWs; this phenomenon was over-amplified in XPS because of its surface sensitivity.

Reaction mechanism

To deduce the transformation mechanism, we assumed that the directions of crystal growth of all reduced products were influenced by the precursor product of V_2O_5 NWs. According to this assumption, we proposed a schematic illustration of a transformative evolution depending on the growth direction of each phase of a VO_x NW. Figure 5 shows the single atomic layers of each phase of VO_x NWs with their corresponding growth plane, determined from the crystalline analyses with HR-TEM and SAED. Figure 5a shows one layer of plane (001) of the V_2O_5 structure; the layer structures along the *b*-axis being the key fragments for the structure in the transformative evolution. During reduction with a reducing gas, the distance between adjacent layers decreased and the layers connected with each other through O–V–O bonds to form a 3D network structure. The lowest oxidation state of vanadium ion was +3 in V_2O_3; two intermediates were found in VO_2(R) and VO_2(B) phases. As a continuous process, the transformation from V_2O_5 to VO_2 (routes *a* and *b*) occurred first; the VO_2 phase then converted further into V_2O_3 (routes *c* and *d*).

In route *a*, the odd layer of V_2O_5 fragment shifted from its original location by −1/4, −1/2, 0. After this dislocation, the odd layers connected with even layers through dangling oxygen atoms; the redundant oxygen atoms were removed by hydrogen molecules. The former layer structures became adjacent to one another, and further new bonds were formed between vanadium and oxygen atoms, resulting in a VO_2(B) phase structure.

In route *c*, the VO_2(B) phase reduced to form the V_2O_3 phase. When the reduction was maintained, VO_2(B) underwent a process similar to route *a*. The fragments of VO_2(B) shifted along the *a*-axis and connected with adjacent ones through originally dangling oxygen atoms. The redundant oxygen atoms again were removed by hydrogen molecules to form the final V_2O_3 structure.

Electronic field emission

The electronic field-emission properties of NWs films as prepared were measured in a vacuum chamber with

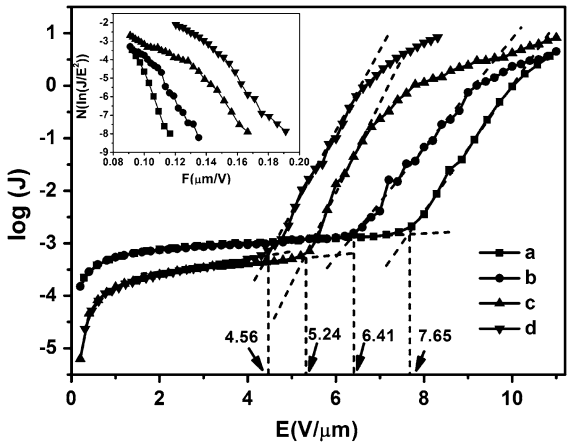

Fig. 6 A semi-log plot of field emission and corresponding Fowler–Nordheim plots (*inset*) of (*a*) V_2O_5, (*b*) VO_2(R), (*c*) VO_2(B), and (*d*) V_2O_3 NW thin films as prepared, respectively

electrodes in a parallel-plate configuration, with a separation of 100 μm between the anodes. Figure 6 reveals the emission current density (J) versus an applied macroscopic field (E) within the range of ~0–1,100 V of bias voltage at a separation of 100 μm between the sample and electrode. The turn-on field (E_{to}), defined by extracting the interception of the linear region to the x-axis of a semi-log plot, and the maximum current density (J_{max}) are summarized in Table 2. The unreduced V_2O_5 NW thin film possessed poor FE properties with $E_{to} = 7.65$ V/μm and $J_{max} = 3.68$ mA/cm^2 at field 11 V/μm. The results revealed that the FE properties were notably improved when the V_2O_5 NWs converted to other reduced vanadium-oxide NWs. The FE properties improved effectively with a decreasing oxidation state. Among these typical products, NWs from the lowest oxidation state V_2O_3 exhibited the best FE properties of $E_{to} = 4.56$ V/μm and $J_{max} = 8.36$ mA/cm^2 at field 8.3 V/μm. The variability of the turn-on field was attributed to the variation of phase and chemical composition.

Table 2 FE properties of product NWs as prepared

	E_{to} (V/μm)	I_{max} (mA/cm)
V_2O_5 NW	7.65	3.68 at 11 V/μm
VO_2(R) NW	6.41	4.50 at 11 V/μm
VO_2(B) NW	5.24	8.21 at 11 V/μm
V_2O_3 NW	4.56	8.36 at 8.3 V/μm

To understand the model for the conduction mechanism from the as synthesized NWs films, a series of data analyses were carried out to find the best model for the electron transfer mechanism of NWs films. The possible current–voltage relations are obtained from the literature by applying suitable mathematical relationship of current and voltage to obtain a straight-line plot (Gonon et al. 1995; May et al. 1998). These models were evaluated with the correlation coefficient (r^2) of the line plot. The results of the analyses for each of the VO_x films are listed in Table 3. The results indicate that for V_2O_5 NWs film, the Fowler–Nordheim model is the best-fit compare to the other models. As the V_2O_5 NWs are reduced, the as synthesized VO_2(R), VO_2(B), and V_2O_3 NWs exhibit better fit models for Poole–Frenkel conduction with overlap of Coulombic potentials, Schottky emission, and space-charge limited currents (SCLC) models, respectively. However, the correlation coefficients for Fowler–Nordheim model are still among the best for these NWs films with r^2 values of 0.93–0.98. According to these results, we propose a possible mechanism for these NWs during the field-emission process. For V_2O_5 NWs films, the electron transfer mechanism is the tunneling of the electrons through the applied potential barrier that follow the Fowler–Nordheim model. For films with reduced VO_x NWs, conduction through the bulk and interfaces may play an important role in the electron transport. The conduction mechanism for reduced form might be a combination of the Fowler–Nordheim surface ejection and other models. A Fowler–Nordheim (F–N) plot of (ln I/E_{to}) versus ($1/E$) appears in the inset of Fig. 6. Further study is necessary to clarify the detail conduction mechanism for the reduced VO_x NWs.

Table 3 Correlation coefficients (r^2) of best linear fit for VO_x NWs films with different types of conduction mechanism

	(1)	(2)	(3)	(4)	(5)	(6)
V_2O_5 NW	0.90	0.99	0.96	0.98	0.82	0.96
VO_2(R) NW	0.96	0.97	0.93	0.93	0.91	0.99
VO_2(B) NW	0.99	0.93	0.97	0.86	0.92	0.96
V_2O_3 NW	0.95	0.98	0.99	0.95	0.88	0.91

Note (1) Schottky emission, (2) Fowler–Nordheim, (3) Space-charge limited currents (SCLC), (4) SCLC with Poole–Frenkel (PF) effect, (5) Poole–Frenkel conduction, (6) Poole–Frenkel conduction with overlap of Coulombic potentials (Hill's law) (Gonon et al. 1995; May et al. 1998)

Conclusion

Reduced products in a series, VO_2(R), VO_2(B), and V_2O_3, were obtained via controlled reduction. A mild reduction condition (10 % H_2, 12 h) favored the formation of pure VO_2(R), whereas rapid reduction (pure H_2, 2 h) yielded VO_2(B). We also demonstrated the single-crystalline properties of reduced vanadium-oxide NWs with a specific growth direction. On the basis of the growth direction of each product, possible mechanisms of conversion during reduction were proposed. All VO_x NWs as obtained possessed interesting field-emission properties, which were influenced by the morphology of the NWs and the nature of the material. Among these NWs, V_2O_3 NWs showed the best FE properties with a turn-on field of 4.56 V/μm and a maximum current density of 8.36 mA/cm^2 at applied field of 11.0 V/μm. Vanadium oxide showed excellent FE properties with a small turn-on field and large maximum current density, which would be useful for field-emission emitters.

Acknowledgments For technical assistance we thank Professor HS Chiu for FET measurements. The National Science Council, Taiwan (contracts NSC 101-2113-M-009-017-MY3) supported this research.

References

Baudrin E, Sudant G, Larcher D, Dunn B, Tarascon JM (2006) Preparation of nanotextured VO_2 B from vanadium oxide aerogels. Chem Mater 18(18):4369–4374

Corr SA, Grossman M, Furman JD, Melot BC, Cheetham AK, Heier KR, Seshadri R (2008) Controlled reduction of vanadium oxide nanoscrolls: crystal structure, morphology, and electrical properties. Chem Mater 20(20): 6396–6404

Fan ZY, Ho JC, Takahashi T, Yerushalmi R, Takei K, Ford AC, Chueh YL, Javey A (2009) Toward the development of printable nanowire electronics and sensors. Adv Mater 21(37):3730–3743

Gonon P, Deneuville A, Fontaine F, Gheeraert E (1995) Electrical-conduction and deep levels in polycrystalline diamond films. J Appl Phys 78(11):6633–6638

Grigorieva AV, Badalyan SM, Goodilin EA, Rumyantseva MN, Gaskov AM, Birkner A, Tretyakov YD (2010) Synthesis, structure, and sensor properties of vanadium pentoxide nanorods. Eur J Inorg Chem 33:5247–5253

Guiton BS, Gu Q, Prieto AL, Gudiksen MS, Park H (2005) Single-crystalline vanadium dioxide nanowires with rectangular cross sections. J Am Chem Soc 127(2):498–499

Ji S, Zhao Y, Zhang F, Jin P (2010) Direct formation of single crystal VO_2(R) nanorods by one-step hydrothermal treatment. J Cryst Growth 312(2):282–286

Jiang Y, Zhang WJ, Jie JS, Meng XM, Zapien JA, Lee ST (2006) Homoepitaxial growth and lasing properties of ZnS nanowire and nanoribbon arrays. Adv Mater 18(12):1527–1532

Jiang JA, Li YY, Liu JP, Huang XT (2011) Building one-dimensional oxide nanostructure arrays on conductive metal substrates for lithium-ion battery anodes. Nanoscale 3(1):45–58

Jiao L, Yuan H, Si Y, Wang Y (2006) Synthesis of Cu0.1-doped vanadium oxide nanotubes and their application as cathode materials for rechargeable magnesium batteries. Electrochem Commun 8(6):1041–1044

Leger C, Bach S, Pereira-Ramos JP (2007) The sol–gel chromium-modified V_6O_{13} as a cathodic material for lithium batteries. J Solid State Electr 11(1):71–76

Li L, Yang YW, Huang XH, Li GH, Ang R, Zhang LD (2006) Fabrication and electronic transport properties of Bi nanotube arrays. Appl Phys Lett 88(10):103119

Li XL, Cai KF, Li H, Yu DH, Wang X, Wang HF (2010) Alumina template-assisted electrodeposition of $Bi_2Te_{2.7}Se_{0.3}$ nanowire arrays. Superlattice Microstruct 47(6):710–713

Liu JF, Wang X, Peng Q, Li YD (2005) Vanadium pentoxide nanobelts: highly selective and stable ethanol sensor materials. Adv Mater 17(6):764

Liu J, Cao GZ, Yang ZG, Wang DH, Dubois D, Zhou XD, Graff GL, Pederson LR, Zhang JG (2008) Oriented nanostructures for energy conversion and storage. ChemSusChem 1(8–9):676–697

May PW, Hohn S, Wang WN, Fox NA (1998) Field emission conduction mechanisms in chemical vapor deposited diamond and diamond-like carbon films. Appl Phys Lett 72(17):2182–2184

Morin F (1959) Oxides which show a metal-to-insulator transition at the Neel temperature. Phys Rev Lett 3(1):34–36

Ramgir NS, Yang Y, Zacharias M (2010) Nanowire-based sensors. Small 6(16):1705–1722

Santulli AC, Xu WQ, Parise JB, Wu LS, Aronson MC, Zhang F, Nam CY, Black CT, Tiano AL, Wong SS (2009) Synthesis and characterization of V_2O_3 nanorods. Phys Chem Chem Phys 11(19):3718–3726

Sediri F, Touati F, Gharbi N (2006) From V_2O_5 foam to VO_2(B) nanoneedles. Mater Sci Eng B 129(1–3):251–255

Wang ZL (2008) Oxide nanobelts and nanowires—growth, properties and applications. J Nanosci Nanotechnol 8(1):27–55

Wang Y, Cao G (2007) Synthesis and electrochemical properties of $InVO_4$ nanotube arrays. J Mater Chem 17(9):894

Wang YQ, Zhang ZJ, Zhu Y, Li ZC, Vajtai R, Ci LJ, Ajayan PM (2008) Nanostructured VO_2 photocatalysts for hydrogen production. ACS Nano 2(7):1492–1496

Wang K, Chen JJ, Zeng ZM, Tarr J, Zhou WL, Zhang Y, Yan YF, Jiang CS, Pern J, Mascarenhas A (2010) Synthesis and photovoltaic effect of vertically aligned ZnO/ZnS core/shell nanowire arrays. Appl Phys Lett 96(12):123105

Wee G, Soh HZ, Cheah YL, Mhaisalkar SG, Srinivasan M (2010) Synthesis and electrochemical properties of electrospun V_2O_5 nanofibers as supercapacitor electrodes. J Mater Chem 20(32):6720

Wei J, Natelson D (2011) Nanostructure studies of strongly correlated materials. Nanoscale 3(9):3509–3521

Wu MC, Lee CS (2009a) Alpha-MoO_3 nanocrystals of controlled size on a glass substrate. Mater Res Bull 44(3): 629–632

Wu MC, Lee CS (2009b) Field emission of vertically aligned V_2O_5 nanowires on an ITO surface prepared with gaseous transport. J Solid State Chem 182(8):2285–2289

Xiong CR, Aliev AE, Gnade B, Balkus KJ (2008) Fabrication of silver vanadium oxide and V_2O_5 nanowires for electrochromics. ACS Nano 2(2):293–301

Yin HH, Luo M, Yu K, Gao YF, Huang R, Zhang ZL, Zeng M, Cao CX, Zhu ZQ (2011) Fabrication and temperature-dependent field-emission properties of bundle-like VO_2 nanostructures. ACS Appl Mater Interfaces 3(6): 2057–2062

Zhai T, Liu H, Li H, Fang X, Liao M, Li L, Zhou H, Koide Y, Bando Y, Golberg D (2010) Centimeter-long V_2O_5 nanowires: from synthesis to field-emission, electrochemical, electrical transport, and photoconductive properties. Adv Mater 22(23):2547–2552

Zhai TY, Li L, Ma Y, Liao MY, Wang X, Fang XS, Yao JN, Bando Y, Golberg D (2011) One-dimensional inorganic nanostructures: synthesis, field-emission and photodetection. Chem Soc Rev 40(5):2986–3004